Eur. Phys. J. B **9**, 431-443 (1999)

THE EUROPEAN PHYSICAL JOURNAL B

EDP Sciences

Dramatic anion size effect on structural and magnetic properties within a series of novel antiferromagnetic organometallic radical cation salts: $[Cp_2Mo(dmit)^{+\bullet}][X^-]$ ($X^- = PF_6^-$, AsF_6^-, SbF_6^-)

R. Clérac[1,a], M. Fourmigué[2], J. Gaultier[3], Y. Barrans[3], P.A. Albouy[4], and C. Coulon[1,b]

[1] Centre de Recherche Paul Pascal, CNRS, avenue du Dr. Schweitzer, 33600 Pessac, France
[2] Institut Jean Rouxel, CNRS-Université de Nantes, 2 rue de la Houssinière, BP 32229, 44322 Nantes Cedex 03, France
[3] Institut de Chimie de la Matière Condensée de Bordeaux, avenue du Dr. Schweitzer, 33600 Pessac, France
[4] Laboratoire de Physique des Solides, CNRS-Université Paris-Sud, Bât. 510, 91405 Orsay Cedex, France

Received 20 July 1998

Abstract. Electrocrystallization of CH_2Cl_2 solutions of $Cp_2Mo(dmit)$, $dmit^{2-}$ = 2-thioxo-1,3-dithiole-4,5-dithiolate, in the presence of n-Bu_4NX ($X^- = PF_6^-$, AsF_6^-, SbF_6^-) affords the corresponding 1:1 cation radical salts $[Cp_2Mo(dmit)^{+\bullet}][X^-]$. The three isostructural salts crystallize in the orthorhombic system, space group Cmcm. In the three salts, a second-order transition at a temperature T_1, identified by EPR measurements and low-temperature X-ray Weissenberg photographs reveals also a splitting of some principal reflections and the twinned character of the crystals, whose room temperature structure may also be described in the monoclinic $P2_1/m$ space group. The second order monoclinic $\rightarrow$ triclinic transition is associated with the apparition of a superlattice characterized by the critical wave vector $\mathbf{q}_1^* = (0, 1/2, 1/2)$ when expressed in the monoclinic system. A second transition at a lower temperature T_2, of first order character, is observed only in the PF_6^- salt. This triclinic $\rightarrow$ triclinic transition leads to a novel superlattice of wave vector $\mathbf{q}_2 = (0, 1/2, 0)$ while the $\mathbf{q}_1^*$ superlattice is conserved down to 10 K in the AsF_6^- and SbF_6^- salts. Finally, a third transition to an antiferromagnetic ground state is observed for the three salts and investigated by static susceptibility measurements and Antiferromagnetic Resonance (AFMR) experiments. The detailed analysis of the AFMR rotation patterns confirms the twinned nature and the low temperature triclinic symmetry of the crystals as well as the peculiar behaviour of the PF_6^- salt, when compared with the two other members of these novel series.

PACS. 76.30.-v Electron paramagnetic resonance and relaxation – 61.50.Ks Crystallographic aspects of phase transformations; pressure effects – 75.50.Ee Antiferromagnetics

1 Introduction

The perhaps most interesting feature of molecular materials lies in our ability to purposely introduce "small" chemical modifications within a given structural pattern while following the evolution of the associated electronic properties of the crystalline solids. As "small" modifications, we can mention for example: (i) the isostructural Bechgaard salts series where the anion substitution (PF_6^-, AsF_6^-, SbF_6^-, ClO_4^-, ReO_4^-, BF_4^-, NO_3^-, SCN^-, Br^-, ...) [1,2] generates a variety of ground states like charge-density-wave (CDW), insulators, spin-density-wave (SDW), superconductivity ...; (ii) the superconducting A_3C_{60} (A: K, Rb, Cs) in which the critical temperature increases continuously with the alcalin cation size [3,4]; (iii) the so-called κ phases of κ-$(BEDT\text{-}TTF)_2Cu[N(CN)_2]X$ salts [5] with a superconducting ground state for X = Br [6], an insulating state for X = Cl [7] and the possibility for both states depending upon the cooling rate in the deuterated $(d_8\text{-}BEDT\text{-}TTF)_2Cu[N(CN)_2]Br$ [8]. These few examples illustrate the crucial role of "small" variations in a given structure on the outcome of the competition between different possible ground states. The anion substitution not only plays the role of an internal pressure effect but also subtly modifies the nature and the strength of the anion-cation interactions [9] controlled by weak Van der Waals and C-H$\cdots$X close contacts. In that respect the discovery of novel series of isostructural compounds exhibiting dramatically different structural and electronic properties is particularly exciting.

[a] *Present address*: Department of Chemistry, Michigan State University, East Lansing, Michigan 48824-1128, USA
[b] e-mail: coulon@crpp.u-bordeaux.fr

While those *planar* molecules such as TTF or BEDT-TTF are well known to organize in the solid state into 1D or 2D conducting and superconducting systems with a strong overlap between donor molecules and hence a sizeable conduction band dispersion, we expect *non-planar* radical molecules to afford original architectures and electronic behaviours. In that respect, metal dithiolene complexes offer a wide variety of molecular structures, bis(dithiolene) square-planar salts such as the prototypical $Ni(dmit)_2^-$ but also tris(dithiolene) complexes with geometries varying from octahedral to trigonal-prismatic depending upon their oxidation state. We recently described [10,11] mixed-ligand complexes which simultaneously incorporate dithiolene and cyclopentadienyl ligands as for example $Cp_2Mo(dddt)$ or $Cp^*Mo(dmit)^-$ where Cp stands for η^5-$C_5H_5^-$, Cp^* for η^5-$Me_5C_5^-$, $dddt^{2-}$ for 5,6-dihydro-1,4-dithiine-2,3-dithiolate and $dmit^{2-}$ for 2-thioxo-1,3-dithiole-4,5-dithiolate. Those diamagnetic $Mo^{(IV)}$ complexes are reversibly oxidized to the corresponding $S = 1/2$ paramagnetic $Mo^{(V)}$ species with a large delocalization of the spin density on the whole molecule. Thus, oxidation of $Cp_2Mo(dddt)$ with TCNQ afforded a 1:1 salt where $Cp_2Mo(dddt)^{+\bullet}$ radical cations organize into alternated chains while oxydation of $Cp_2Mo(dmid)$, $dmid^{2-}$ for 2-oxo-1,3-dithiole-4,5-dithiolate, with $TCNQF_4$ gives rise to original spin ladder systems [10]. Those results demonstrate the potentialities of this class of complexes for the elaboration of novel materials with interesting magnetic properties.

In this paper, we report on a series of isostructural cation-radical salts of $Cp_2Mo(dmit)$ with the small, closed-shell, octahedral anions PF_6^-, AsF_6^- and SbF_6^-. Combined with the room temperature structure analysis of the pertinent intermolecular interactions, the low temperature structural and magnetic (both static and dynamic) studies reveal a clear separation between the PF_6^- salt in one hand and the AsF_6^- and SbF_6^- salts in the other hand. This dramatic anion size effect on the structural and magnetic properties will be described and discussed.

2 An isostructural series of organometallic 1:1 cations radical salts: structure analysis

$Cp_2Mo(dmit)$ [11] was prepared as described earlier from the reaction of Cp_2MoCl_2 and the dianionic dithiolene in refluxing THF. Electrocrystallization experiments of $Cp_2Mo(dmit)$ with 0.05M CH_2Cl_2 solutions of n-$Bu_4N^+AsF_6^-$ as electrolyte afforded the 1:1 salt $[Cp_2Mo(dmit)]AsF_6$ in the form of elongated plates growing directly on the platinum electrode. Substitution of n-$Bu_4N^+PF_6^-$ or n-$Bu_4N^+SbF_6^-$ for n-$Bu_4N^+AsF_6^-$ as electrolyte afforded the corresponding 1:1 $Cp_2Mo(dmit)^{+\bullet}$ PF_6^- and SbF_6^- salts with these respectively smaller and larger anions. X-ray crystal structure determinations [12] were conducted at room temperature for the three salts. They are isostructural and crystallize in the orthorhombic system, space group Cmcm

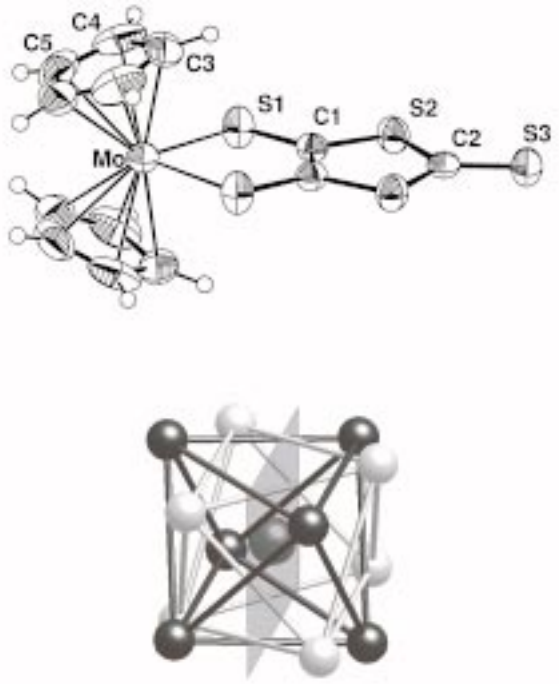

Fig. 1. ORTEP view of $Cp_2Mo(dmit)^{+\bullet}$ in $[Cp_2Mo(dmit)^{+\bullet}][X^-]$ and representation of the two positions of the disordered octahedral anion.

(Tab. 1). The $Cp_2Mo(dithiolene)^{+\bullet}$ and X^- moieties (Fig. 1) have the crystallographic site symmetry m2m. The whole Mo(dmit) moiety lies on the mirror plane perpendicular to the [100] direction while the octaedral anion is disordered on two positions related by the mirror plane perpendicular to the [001] direction. Final positional and equivalent thermal parameters for the three salts are given in Table 2.

In the solid state, the $Cp_2Mo(dithiolene)^{+\bullet}$ cations are organized into layers in the (ab) plane (Fig. 2). Within one layer, the dithiolene moieties all point in the same direction (and in the next layer toward the opposite direction). The shortest *intermolecular* cation/cation distances within one layer are found between the cyclopentadienyl and the outer sulfur atom (S3), each molecule being surrounded by four such equivalent neighbours in the (ab) plane (interaction 1). Moreover any given $Cp_2Mo(dithiolene)^{+\bullet}$ cation overlaps with two sets of molecules of the neighbouring layers. A S-S interaction between two coplanar dithiolene moieties develops along the c direction (interaction 2) while along the $a+c$ and $a-c$ directions, the interaction is attributable to Cp/(S1/S2) short contacts (interaction 3). We are thus able to identify for each molecule, a set of ten neighbours (4 in the (ab) plane, 2 along the c direction and 4 in the (ac) plane), establishing a fully three-dimensional structure for those paramagnetic salts.

The strength of the cation/cation intermolecular interactions associated with those short contacts can be quantified by extended Hückel calculations [13] of the associated interaction energies $2t$ (Tab. 3), defined as the energy difference between the HOMO and HOMO-1

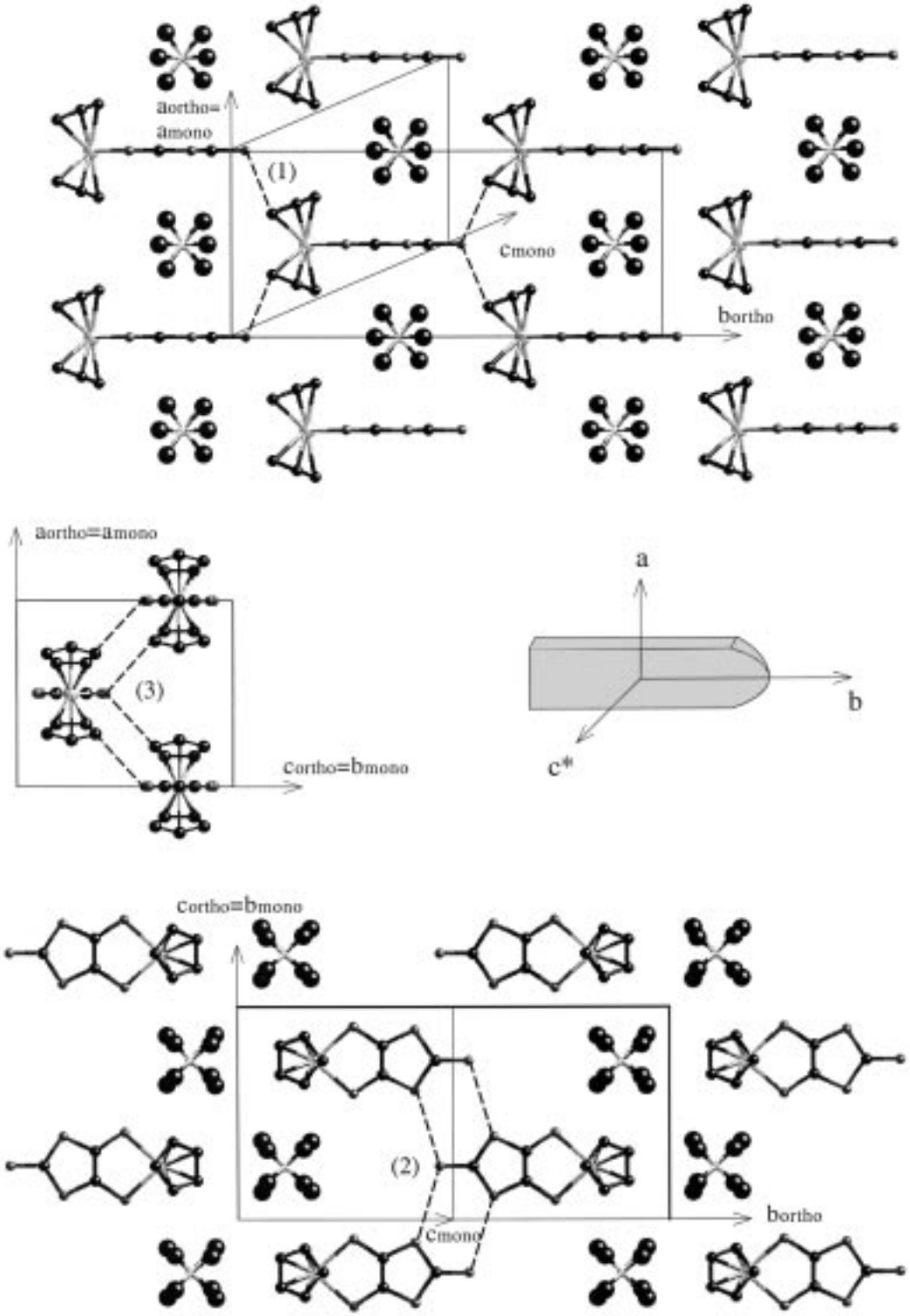

Fig. 2. Views of the unit cell of the $[Cp_2Mo(dmit)^{+\bullet}][AsF_6^-]$ compound, in the two different symmetries (orthorhombic and monoclinic). Anions have been omitted for clarity in the central figure. The three relevant intermolecular interactions (1), (2), (3) have been represented as dotted lines. The crystallographic axes have been positionned on a crystal drawing with the usual morphology (typical crystal dimensions: $1.0 \times 0.2 \times 0.03$ mm^3).

Table 1. Crystallographic data for $[Cp_2Mo(dmit)]X$.

	$Cp_2Mo(dmit)PF_6$	$Cp_2Mo(dmit)AsF_6$	$Cp_2Mo(dmit)SbF_6$
formula	C13H10S5MoPF6	C13H10S5MoAsF6	C13H10S5MoSbF6
color, habit	black platelet	black platelet	black platelet
crystal size /mm	$0.36 \times 0.09 \times 0.03$	$0.45 \times 0.15 \times 0.03$	$0.33 \times 0.12 \times 0.015$
M_r/g mol^{-1}	567.457	611.404	658.240
temperature /K	293	293	293
crystal system	orthorhombic	orthorhombic	orthorhombic
space group (no.)	Cmcm (63)	Cmcm (63)	Cmcm (63)
a/Å	8.9520(9)	8.9779(9)	9.0580(9)
b/Å	20.602(2)	20.647(2)	20.819(2)
c/Å	10.104(1)	10.225(1)	10.388(1)
V/Å^3	1863.5(3)	1895.5(3)	1959.0(3)
Z	4	4	4
d_{calc}/g cm^{-3}	2.023	2.142	2.232
μ/mm^{-1}	1.4	3.03	2.6
diffractometer	CAD4F	CAD4F	Siemens P4
2θ range/degrees	4–52	4–52	4–60
scan type	$\omega - 2\theta$	$\omega - 2\theta$	ω
data collected	7611	2165	6308
index ranges	$\pm h$, $\pm k$, $\pm l$	$+h$, $+k$, $+l$	$-h$, $\pm k$, l
	11, 25, 12	11, 25, 12	12, 29, 14
independent data	1061	1083	1626
R_{int}	0.0467	0.041	0.0647
observed data	782	767	1626
($I_{obs} > 2\sigma(I)$)			
param. refined	F	F	F
refl. in refin.	1046	776	1024
no of param.	89	89	89
R [a], R_w [b]	0.064, 0.084	0.044, 0.056	0.045, 0.057
S [c]	1.51	1.05	0.96
res. density/eÅ^{-3}	−0.85, 0.86	−1.07, 0.99	−1.24, 0.97

[a] $R = \Sigma||F_o| - |F_c||/\Sigma|F_o|$.
[b] $R_w = [\Sigma w(|F_o| - |F_c|)^2/\Sigma w|F_o|^2]^{1/2}$.
[c] $S = [\Sigma w(F_o^2 - F_c^2)^2/(N_{obs} - N_{var})]^{1/2}$.

frontier orbitals of the supermolecule made of two interacting $[Cp_2Mo(dithiolene)]_2$ moieties. As shown in Table 3, weak overlaps are formed in both directions and no particular trend is to be noted in the evolution of interaction 1 with the anion change while a clear decrease of interactions 2 and 3 is observed when going from the smaller PF_6^- to the larger AsF_6^- and SbF_6^-. The evolution of the unit cell parameters (Tab. 4) within the series (PF_6^- *vs.* AsF_6^- *vs.* SbF_6^-) shows that the anion size controls the compacity of the structure along the c direction. As a consequence, calculated interactions 2 (along c) and 3 (along $a+c$, $a-c$) exhibit a clear dependence with the anion size.

These series offer thus a unique opportunity to investigate the effect of the anion size on the intermolecular interaction network. Its variations upon anion substitution is expected to play a crucial role in the evolution of the electronic properties of those three paramagnetic salts. In the following, we will describe and compare their structural and magnetic behaviours between room temperature and 2 K.

3 Static magnetism

Magnetic susceptibility measurements were performed on polycrystalline samples with a Quantum Design MPMS-5 SQUID magnetometer operating in the range 1.7-300 K. The three salts exhibit a similar temperature dependence with a Curie Weiss behaviour [14] down to 30 K

Table 2. Atomic positional and isotropic thermal parameters for $[Cp_2Mo(dmit)]X$.

	x/a	y/b	z/c	U_{eq}
$[Cp_2Mo(dmit)]PF_6$:				
Mo	0.5	0.17500(4)	0.75	0.0348(6)
S1	0.5	0.2635(1)	0.5885(2)	0.047(1)
S2	0.5	0.4075(1)	0.6068(2)	0.042(1)
S3	0.5	0.5332(2)	0.75	0.052(2)
C1	0.5	0.3318(4)	0.6815(8))	0.036(4)
C2	0.5	0.4548(6)	0.75	0.039(6)
C3	0.753(1)	0.1903(5)	0.75	0.070(7)
C4	0.7171(9)	0.1520(5)	0.6373(8)	0.068(5)
C5	0.6654(8)	0.0943(4)	0.6824(9)	0.069(5)
P	0.	0.3899(2)	0.75	0.044(2)
F1	0.	0.4414(8)	0.638(2)	0.10(1)
F2	0.	0.339(1)	0.645(2)	0.13(2)
F3	0.120(2)	0.351(1)	0.674(2)	0.15(2)
F4	−0.118(2)	0.430(1)	0.681(2)	0.17(2)
$[Cp_2Mo(dmit)]AsF_6$:				
Mo	0.5	0.17679(4)	0.75	0.0367(5)
S1	0.5	0.2649(1)	0.5909(2)	0.048(1)
S2	0.5	0.4088(1)	0.6084(2)	0.045(1)
S3	0.5	0.5339(2)	0.75	0.057(2)
C1	0.5	0.3336(4)	0.6810(8)	0.035(4)
C2	0.5	0.4561(6)	0.75	0.040(6)
C3	0.750(1)	0.1933(6)	0.75	0.086(8)
C4	0.7166(8)	0.1525(5)	0.6380(7)	0.072(5)
C5	0.6639(8)	0.0965(4)	0.6817(8)	0.073(5)
As	0.	0.39048(6)	0.75	0.0419(7)
F1	0.	0.4455(9)	0.630(2)	0.11(1)
F2	0.	0.3335(9)	0.635(2)	0.14(2)
F3	0.132(2)	0.3506(8)	0.668(2)	0.15(1)
F4	−0.125(2)	0.4356(9)	0.674(2)	0.16(1)
$[Cp_2Mo(dmit)]SbF_6$:				
Mo	0.5	0.17937(5)	0.75	0.0425(5)
S1	0.5	0.2672(1)	0.5934(2)	0.054(1)
S2	0.5	0.4100(1)	0.6104(3)	0.054(1)
S3	0.5	0.5342(2)	0.75	0.071(3)
C1	0.5	0.3352(4)	0.6815(9)	0.043(4)
C2	0.5	0.4567(6)	0.75	0.048(7)
C3	0.748(1)	0.1943(6)	0.75	0.091(9)
C4	0.715(1)	0.1560(5)	0.6401(8)	0.080(6)
C5	0.6635(8)	0.0995(4)	0.6834(9)	0.074(5)
Sb	0.	0.39209(4)	0.75	0.0472(5)
F1	0.	0.4526(8)	0.622(2)	0.13(2)
F2	0.	0.330(1)	0.628(2)	0.18(3)
F3	0.142(2)	0.3479(8)	0.662(2)	0.15(1)
F4	−0.141(2)	0.4383(8)	0.664(2)	0.15(1)

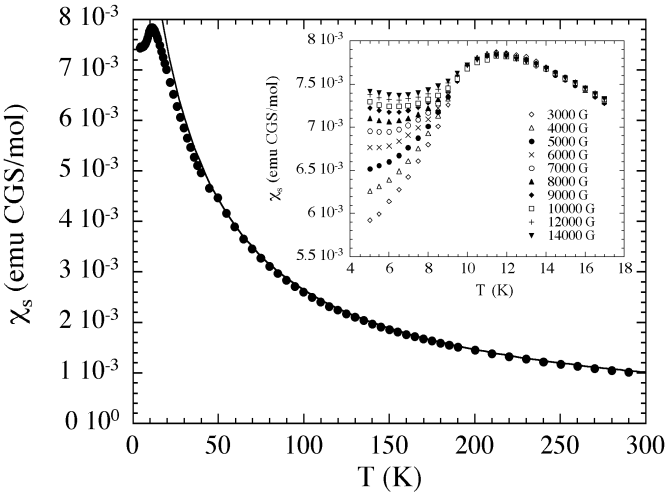

Fig. 3. Temperature dependence of the static susceptibility $\chi_s = (M/B)$ at 5 T in $[Cp_2Mo(dmit)^{+\bullet}][AsF_6^-]$. Data have been corrected for diamagnetism: In insert: low temperature magnetic susceptibility in various fields. The solid line is the fit to the Curie-Weiss law for $T > 30$ K with $\theta = -21 \pm 1$ K.

and $\theta = -37$ K, -21 K and -14 K in the PF_6^-, AsF_6^- and SbF_6^- salts respectively. For example, Figure 3 gives the temperature dependence of the "static" susceptibility $\chi_s = M/B$ when the applied magnetic field is 5 T. The continuous line gives the fit with the Curie Weiss law. Note that the largest θ and T_N values (Tab. 5) are obtained with the smallest anions. Indeed, the strongest interactions are expected in the PF_6^- salt where the organic moieties are closest to each other, as confirmed by the calculated ($2t$) interaction energies mentionned above. In a Hubbard model, the J values are directly related to $2t$ ($J \approx 2t^2/U$ where U is the intrasite electronic repulsion term). From the calculated $2t$ values and a standard $U = 1$ eV [15,16], the summation of the three intermolecular interaction energies (J_1, J_2 and J_3), compares favorably with the Weiss temperature θ.

Let us now describe the low temperature behaviour in more details. We give in insert of Figure 3 the example of the AsF_6^- salt. As expected, the magnetic susceptibility is independent of the applied magnetic field in the paramagnetic phase above 10 K. Below 20 K, a clear departure from the Curie-Weiss behaviour is observed and $\chi_s = M/B$ reaches a maximum at about 11 K. Below 9.5 K, a field dependence is found, characteristic of the occurrence of an antiferromagnetic ground state. To discuss this dependence and extract the corresponding characteristic field, the easiest way is *a priori* a plot of the "differential" susceptibility $\chi_d = \partial M/\partial B$ *vs.* B at different temperatures. In fact, Uyeda and Date [17] have estimated χ_d for a powder sample in the antiferromagnetic phase. Starting from the mean field Nagamiya theory, the orientation of the magnetic moment and the corresponding net magnetization can be obtained for a given orientation of the magnetic field. The next step is an average over the field orientation to simulate the powder result. A maximum of χ_d is obtained at the characteristic field $B_c = \sqrt{2K_1 J}$ (K_1 is the easy-intermediate anisotropy and

Table 3. Calculated intermolecular interaction energies ($2t$), in meV and their sum in K.

	Interaction (1)	Interaction (2)	Interaction (3)	$\sum$ Interactions
$Cp_2Mo(dmit)PF_6$	49.0	25.6	37.3	27
$Cp_2Mo(dmit)AsF_6$	43.7	24.1	33.3	21
$Cp_2Mo(dmit)SbF_6$	45.3	21.1	27.2	13

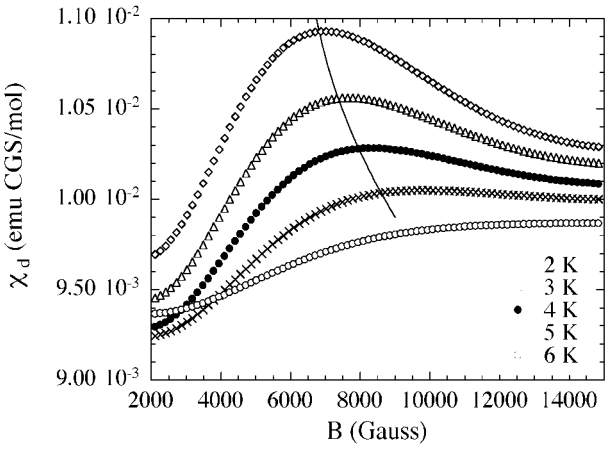

Fig. 4. Field dependence of the differential susceptibility $\chi_d = (\partial M/\partial B)$ at different temperatures in the antiferromagnetic state of $[Cp_2Mo(dmit)^{+\bullet}][AsF_6^-]$. The solid line shows the temperature dependence of the characteristic field of the antiferromagnetic state.

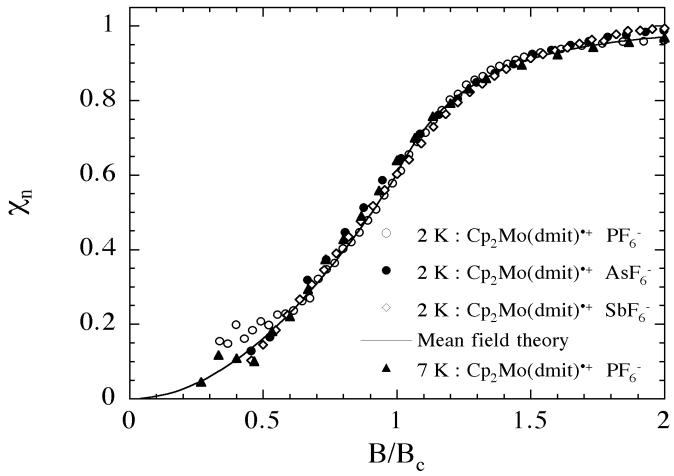

Fig. 5. Evolutions of χ_n (defined in the main text) *vs.* B/B_c for the AsF_6^- and SbF_6^- salts at 2 K and for the PF_6^- salt at 2 and 7 K. The solid line shows the mean-field theoretical result.

Table 4. Evolution of the unit cell parameters with $[Cp_2Mo(dmit)]AsF_6$ taken as reference.

	δa (%)	δb (%)	δc (%)
$Cp_2Mo(dmit)PF_6$	−0.2	−0.2	−1.2
$Cp_2Mo(dmit)AsF_6$	—	—	—
$Cp_2Mo(dmit)SbF_6$	+0.8	+0.8	+1.6

J the exchange energy) which gives the spin-flop field when extrapolated at zero temperature. As we measure the magnetization, we should deduce χ_d from numerical derivation. The result is given in Figure 4. A maximum is in fact observed which gives the temperature dependence of the characteristic field B_c (continuous line in Fig. 4). The extrapolation to 0 K gives the spin-flop field $B_{SF} = 6500 \pm 250$ G.

For a more detailed discussion of the data, the previous strategy is limited as the numerical derivation may introduce deformations of χ_d *vs.* B, in particular close to the maximum. Moreover, it is interesting to introduce a normalized plot to compare data from different compounds and at different temperatures. For this reason, we have introduced the normalized susceptibility $\chi_n = (\chi_s(B) - \chi_s(B=0))/(\chi_s(B \gg B_c) - \chi_s(B=0))$ where $\chi_s(B)$ is the static susceptibility at a given field. As χ_s *vs.* B saturates when B is much larger than B_c, we use this limit together with the extrapolation of χ_s at $B = 0$ to normalize the data. As shown in Figure 5, a unique figure is obtained when χ_n is plotted *vs.* the reduced variable B/B_c. This result is also independent of the temperature in the antiferromagnetic phase. To compare with the Uyeda and Date calculation, we have deduced by the same technique the theoretical estimation of χ_n *vs.* B/B_c (solid line in Fig. 5). Our data for the three salts are totally consistent with this theoretical prediction.

After this characterization, we propose in the following a more detailled study based on a combination of EPR and X-ray diffraction studies. Moreover, the low temperature antiferromagnetic ground state will be characterized by antiferromagnetic resonance experiments (AFMR) in the second part of this paper.

4 The paramagnetic phase

EPR experiments were performed on oriented single crystals on a Brucker ESP300E spectrometer equipped with a ESR900 cryostat (4.2-300 K) from Oxford Instruments. A unique Lorentzian line is systematically observed, its integration gives the temperature dependence of the spin susceptibility which is consistent with the static measurements (SQUID magnetometer) described above. The eigenvalues of the g tensor are found along the crystal principal axes (a, b and c) as expected from the orthorhombic symmetry [18]. Those values are almost identical for the three compounds [19] and, we obtain for example $g_a = 1.9999$, $g_b = 2.0276$ and $g_c = 2.0133$ for the PF_6^- salt. Both eigenvalues and principal magnetic axes are temperature independent (Figs. 6 and 7). Small anomalies can however be observed (Fig. 6) which can be correlated to the linewidth (ΔH) temperature dependence. Indeed, as shown in Figure 8, several anomalies such as inflexion points or discontinuities are clearly identified in the $\Delta H = f(T)$ plots.

Table 5. Magnetic parameters obtained by static susceptibility measurements for $[Cp_2Modmit^{+\bullet}][X^-]$.

	T_N (K)	θ (K)	C/C_0	B_{SF} (Gauss)
$[Cp_2Modmit^{+\bullet}][PF_6^-]$	11.5 ± 0.5	−37 ± 1	0.7 ± 0.1	7000 ± 150
$[Cp_2Modmit^{+\bullet}][AsF_6^-]$	9.5 ± 0.5	−21 ± 1	0.9 ± 0.1	6500 ± 150
$[Cp_2Modmit^{+\bullet}][SbF_6^-]$	7.5 ± 0.5	−14 ± 1	1.0 ± 0.1	6200 ± 150

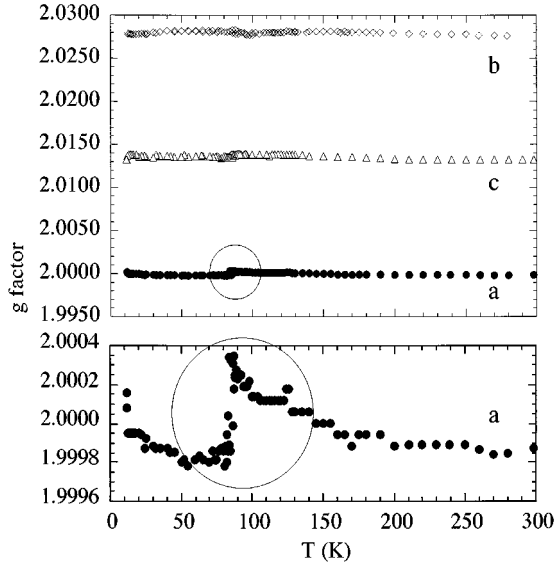

Fig. 6. Temperature dependence of the g factor in the three principal directions of the PF_6^- salt. The bottom figure represents an enlargement in the a_{ortho} direction.

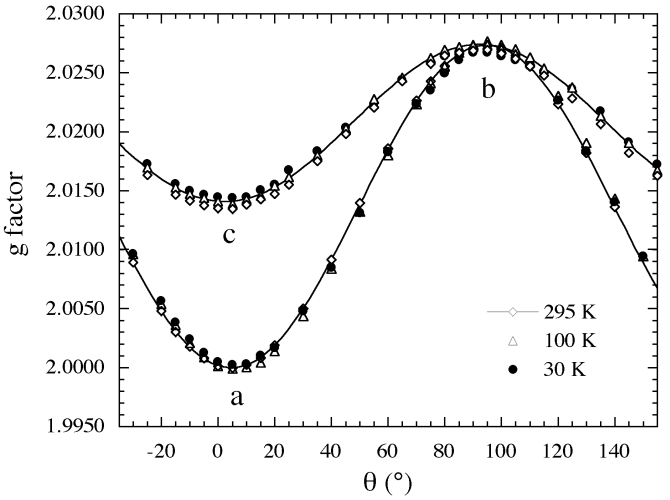

Fig. 7. Rotation pattern of g factor in the two principal planes $(ab)_{ortho}$ and $(bc)_{ortho}$ at 300 K, 100 K and 30 K of the PF_6^- salt. The solid lines are sinusoidal fits.

First, the EPR signal narrows below 15-20 K and finally disappears at the Neel temperature. Close to this magnetic ordering, we expect to see precursors effects, in particular on the linewidth. These critical effects have been already discussed in organic conductors taking the example of the Bechgaard salts [20]. The usual case with no anion ordering involved has been documented

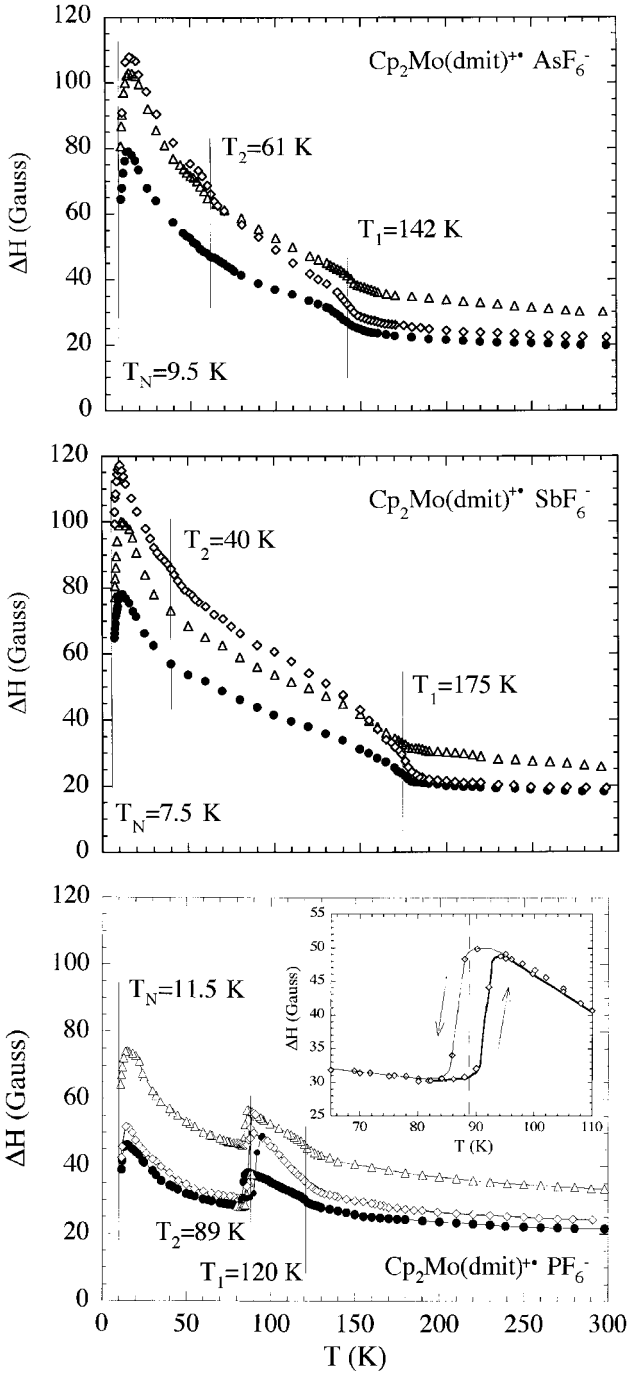

Fig. 8. Temperature dependence of the EPR linewidth in the three principal directions (• along a_{ortho}, ◇ along b_{ortho}, △ along c_{ortho}) for the three salts. In insert of the bottom figure: the hysteresis of the linewidth temperature dependence. The solid line is a guide to the eyes.

experimentally. A divergence of the EPR linewidth is found which has been explained theoretically in the frame of a 3-d RPA theory. In the present case, we rather observe a decrease of the linewidth approaching the Néel temperature. However, we should consider the effect of the observed structural phase transitions as they strongly affect the spin relaxation (in particular in the case of the AsF_6^- or SbF_6^- salts). A similar example is given by $(TMTTF)_2SCN$ where both an anion (at $T_{AO} = 160$ K) and an antiferromagnetic ordering (at $T_N = 7$ K) are observed [21]. In that case, a decrease of the EPR linewidth is first observed before the usual divergence. Note that in the paramagnetic phase at about 20 K, the EPR linewidth is typically two times larger than in other TMTTF salts (like $(TMTTF)_2SbF_6$), indicating an important effect of the anion ordering on the spin relaxation. On the other hand, the linewidth of the antiferromagnetic resonance is similar in $(TMTTF)_2SCN$ and $(TMTTF)_2SbF_6$ (of the order of 80 G along the easy axis [22]). This result strongly suggests that the origin of the relaxation is different in the paramagnetic and antiferromagnetic phases. In that case, the observed decrease of the EPR linewidth illustrates the crossover between these two regimes. We think that a similar discussion applies for the present compounds although we only observe a decrease of the EPR linewidth. It might be that the expected divergence occurs too close to T_N to be observed in our experiment. To support this discussion, it is finally interesting to note that the antiferromagnetic resonance in the present series has a linewidth (close to the easy axis) of 50-100 G, *i.e.* a value similar to the one observed in other organic sulfur compounds although the EPR linewidth was very different.

Besides this signature of the antiferromagnetic ground state, two inflexion points are also observed respectively at $T_1 = 142$ K and $T_2 = 61$ K in the AsF_6^- and $T_1 = 175$ K and $T_2 = 40$ K in the SbF_6^- salt. In the PF_6^- salt an inflexion point at $T_1 = 120$ K is followed by an abrupt decrease of ΔH at about $T_2 = 89$ K. The presence of hysteresis (insert of Fig. 8c) around this last temperature demonstrates unambiguously the first order character of this transition observed only in the PF_6^- salt. This peculiar behaviour, when compared with the AsF_6^- and the SbF_6^- compounds, makes these series particularly exciting. Although the linewidth provides dynamic informations (on the spin relaxation), anomalies in its temperature dependence often reveals thermodynamic instabilities such as structural phase transitions [23–25] and the EPR results therefore suggest the existence of structural phase transition in the paramagnetic domain. One question now arises: why those three *isostructural* salts behave so differently? In order to clarified this point, detailled low temperature X-ray studies were performed on the PF_6^- and the AsF_6^- salts.

Two types of experiments were conducted in different temperature ranges on two diffractometers with low-temperature Helium cryostats allowing a temperature control between 300 and 10 K, (i) rotating-crystal (around the c_{ortho} axis) and Weissenberg photographs on a home-made diffractometer with an oscillating radial collimator to reduce Be diffusion, (ii) rotating-crystal experiments (around the c_{ortho} axis) on a diffractometer with a linear detector, allowing the measurements of precise intensity data and their evolution with the temperature. Rotating-crystal and Weissenberg photographs taken at room temperature confirm the orthorhombic space group and the cell C centering for the three compounds. Below 100 K in the PF_6 salt and at 126 K in the AsF_6 salt, *i.e.* below the first ΔH anomaly temperature (T_1), two important features are identified. On one hand, some of the principal reflections appear to be splitted into two spots of equivalent intensity, showing that these crystals are systematically twinned in this temperature range. Moreover, satellite peaks are now observed between the principal layers, indicative of the apparition of a superlattice. This clearly indicates that the T_1 anomaly can be associated in both salts with a structural phase transition. Note that we have not investigated the nature of precursor effects because this study requires a more sensitive technique. Let us discuss separately those two experimental observations.

4.1 Analysis of the twinned structure

As mentioned above, X-rays reveals below T_1 a splitting of some Bragg spots in addition to the observation of satellites. This former observation cannot be explained as a natural consequence of the occurence of a superlattice. The simplest interpretation for this splitting is the existence of a systematic twinning of the crystals below T_1. The crystallographic analysis of the X-rays data has therefore been performed considering that each set of spots is associated to one single crystal. In that case, the symmetry of each of the two twins should be described in a triclinic $P\bar{1}$ space group.

At this point two competing assumptions are possible: i) the structural phase transition occuring at T_1 induces the twinning ; ii) the twinning is already present (although not observed) above T_1, *i.e.* the two sets of Bragg spots are not separated but already present. In the latter case, the observed C centered orthorhombic room temperature structure would not be deduced from a single crystal. This orthorhombic lattice could be described as a rigorous superposition of two monoclinic lattices with antiparallel a^* and b^* axes and the same c^* axis (see Fig. 9). The two corresponding monoclinic cells correspond to each other through a two fold axis parallel to b_{ortho} or through a mirror plane perpendicular to b_{ortho}. The monoclinic space group would be then $P2_1/m$, with a direct unit cell twice as small as the orthorhombic one, and without the mirror plane containing the whole Mo(dmit) moiety. In this description the whole Mo(dmit) moiety is not necessarily planar (as it should be in the orthorhombic description) which is certainly a more reliable assumption [9]. However we have presently no direct evidence for a twinning of the crystals at room temperature.

In any case, we will use in the following the monoclinic description which is more appropriate to the description of the physical properties.

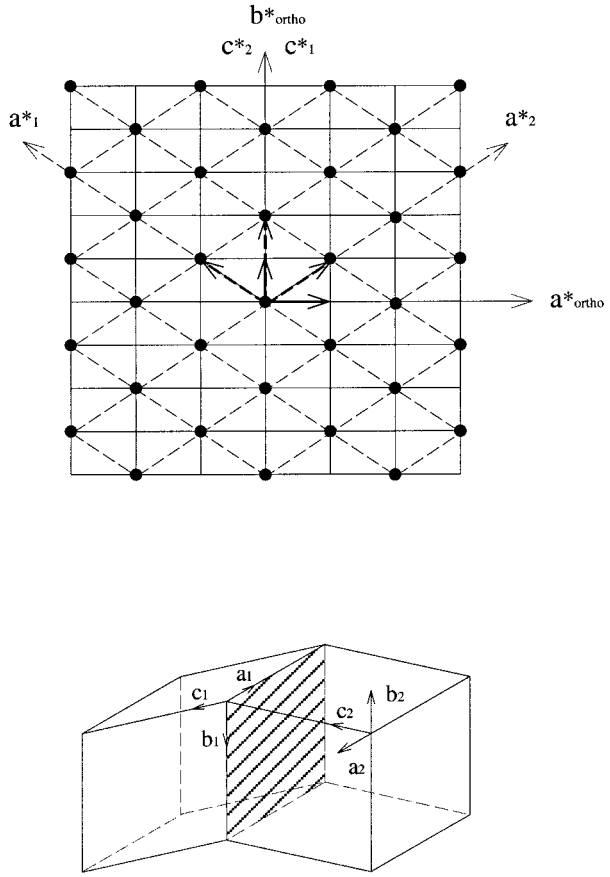

Fig. 9. Top: decomposition of the orthorhombic reciprocal lattice in two monoclinic reciprocal lattices. Bottom: description of the twinned structure in the real space.

As far as the T_1 structural phase transition is concerned, Figure 10 shows that observed increasing splitting of the principal reflexions along the b^* axis implies that α^* deviate from 90° in the low temperature triclinic structure while the absence of any splitting along the a^* axis indicates that β^* is almost temperature independent. The new symmetry below T_1 is then triclinic.

4.2 Analysis of the superlattice

As we already mentioned, this transition is also accompanied by the apparition of satellite peaks. Rotating-crystal and Weissenberg photographs provide the unambigous superlattice description (in the monoclinic system) with a modulation vector $\mathbf{q}_1^* = (0, 1/2, 1/2)$, for both salts. Although no real extinction occurs in the $P\bar{1}$ space symmetry, Bragg spot with $h'+l' = 2n$ (where h', k', l' are Miller indices for the new triclinic lattice) are not observable. This pseudo-extinction is related to a pseudo A centering of the triclinic unit cell, a reminiscence of the former symmetry center of the original monoclinic cell.

In the AsF_6^- salt, the intensity of the (0,1/2,1/2) satellites increases continuously with decreasing temperature (Fig. 11), an indication for a second-order transition. These superlattice spots are still observed at 10 K and their intensity exibits no anomaly while crossing T_2 (61 K). Therefore, the T_2 magnetic anomaly does not appear to be related to a structural phase transition in this salt.

In the PF_6^- salt, the same (0,1/2,1/2) superlattice is observed but it disappears abruptly at $T_2 = 89$ K while a novel triclinic superlattice, of modulation vector $\mathbf{q}_2 = (0, 1/2, 0)$, is now observed. As shown in Figure 12, the intensity of those $\mathbf{q}_2$ satellite peaks is already strong at T_2 (89 K), confirming the first-order character of this phase transition, as already inferred from the EPR studies (see above). It does not change upon further cooling and persists down to 10 K.

In conclusion, the two room temperature isotructural PF_6^- and AsF_6^- salts exibit a strickingly different behaviour at low temperature. While in the AsF_6^- compound, we identified only one second order structural transition at T_1 (142 K) with a critical wave vector $\mathbf{q}_1^* = (0, 1/2, 1/2)$, in the PF_6^- compound, the second order transition at T_1 (120 K) with the same wave vector $\mathbf{q}_1^*$ is followed by a first order structural transition at T_2 (≈ 89 K) with a new critical wave vector $\mathbf{q}_2 = (0, 1/2, 0)$. The close relationship between the magnetic behaviour of the AsF_6^- and SbF_6^- salts allows us to infer that the SbF_6^- salt probably exhibits structural characteristics similar to those of the AsF_6^- one. This point will be further reinforced by the following antiferromagnetic resonance studies.

5 Antiferromagnetic resonance, dynamic investigation of the ground state

As the EPR linewidth remains comparable to those obtained in other organic donors [26–28] as well as in related molybdenum complexes [29], one expects to be able to observe the antiferromagnetic resonance with a conventional X-band EPR spectrometer. The quantitative analysis of AFMR rotation patterns has been recently investigated to provide information on the magnetic anisotropy in a variety of molecular antiferromagnetic systems [30,31]. The study consists in rotating a single crystal around simple magnetic axes at fixed temperature (4 K) to generate resonance field rotation patterns. In the present case, the crystallographic axes of the room temperature structure are easily located from the crystal symmetry (Fig. 13). The long axis of the crystal corresponds to the b_{mono} axis. The c^*_{mono} axis is perpendicular to the platelet plane.

The crystal was first rotated around the a_{mono} *i.e.* in the $(bc^*)_{\mathrm{mono}}$ plane. As shown in Figure 14, two antiferromagnetic resonances were in fact observed in this plane with the extrema of the rotation pattern when the magnetic field is along two directions E_1 and E_2 symmetrically separated from the b_{mono} axis by α and $-\alpha$ respectively (Fig. 14). The presence of characteristic "bubble" rotation patterns in the $(bc^*)_{\mathrm{mono}}$ plane indicates unambiguously that the plane is the Easy/Intermediate plane and that the experimental frequency ω_0 (9.4 GHz) is smaller than the characteristic frequency Ω_- [28]. Moreover, the existence of two "bubbles" implies the presence of two easy axes E_1 and E_2, a clear signature of the crystal

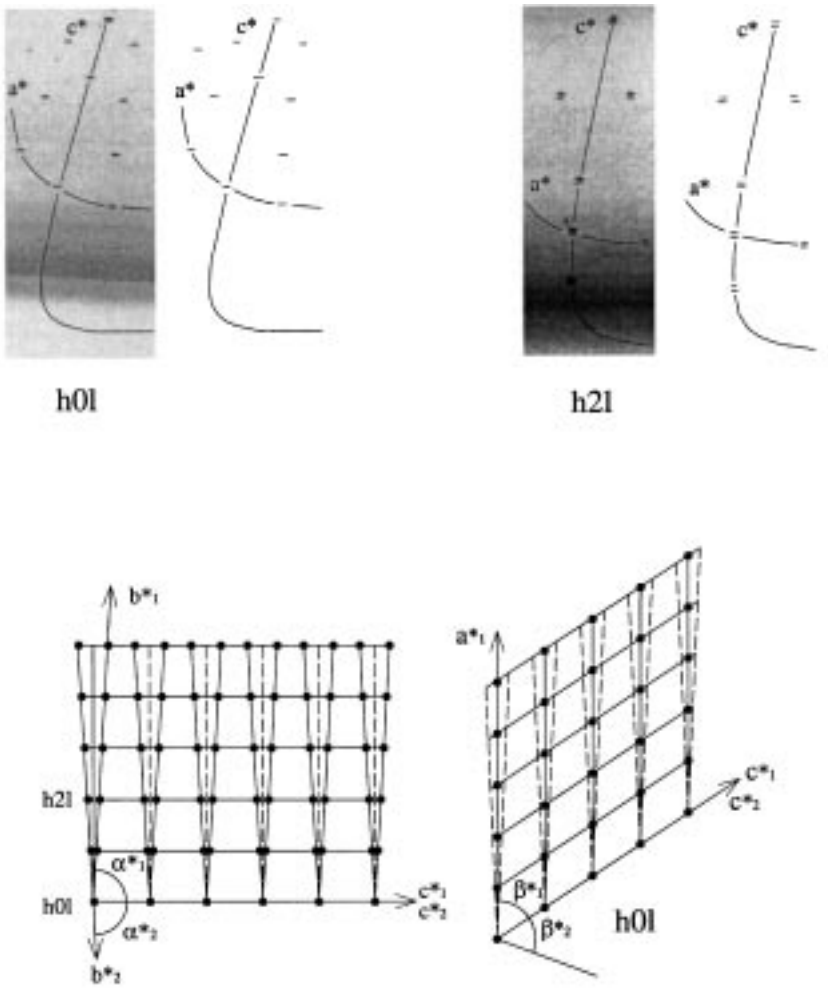

Fig. 10. Top: Weissenberg photographs of the $h0l$ and $h2l$ planes at 10 K for $[Cp_2Mo(dmit)^{+\bullet}][AsF_6^-]$. Note that no splitting is observed in the $h0l$ plane. Bottom left: splitting of the monoclinic reciprocal lattice into two triclinic reciprocal lattices. The increasing separation of the reflexions with increasing k values implies that α_1^* and α_2^* differ from 90°. Bottom right: the absence of splitting in the $h0l$ plane implies that β_1^* and β_2^* do not differ significantly from the monoclinic value.

twinning, each of the two elements of the twin contributing to one single rotation figure. Furthermore, the Hard axis is necessarily perpendicular to the $(bc^*)_{\mathrm{mono}}$ plane (the Easy/Intermediate plane) *i.e.* along a, as confirmed by the rotation pattern in the (E_1, a) plane (Fig. 14), characteristic of an Easy/Hard rotation with $\omega_0 < \Omega_-$. This orientation of the magnetic frame confirms thus the existence of a structural phase transition. Keeping the monoclinic symmetry would impose the coincidence of the monoclinic axis with one of the magnetic axes. Here, it would require the a axis to become the monoclinic one, an highly improbable feature, thus confirming the low temperature triclinic symmetry already identified from the X-ray experiments described above.

The shape of the rotation figures is similar for the three compounds confirming the common low temperature triclinic symmetry. The $(\mathbf{b}, \mathbf{E}_{\mathrm{i}})$ angle, α, amounts to $39 \pm 1°$ in the AsF_6^- salt (Fig. 14) and to $42 \pm 1°$ in the SbF_6^- while a value of $9 \pm 1°$ is determined from the rotation pattern of the PF_6^- compound (Fig. 15). We thus observe that the two former salts incorporating the larger anions (AsF_6^- and SbF_6^-) with the same low temperature superlattice ($\mathbf{q}_1^*$) exhibit similar α values while the PF_6^- salt with a different superlattice ($\mathbf{q}_2$) presents a much smaller α value.

These experimental results can be fitted using the AFMR theory [32,33]. The solid lines in Figures 14, give examples of best fits imposing that the three main parameters r, Ω_- and Ω_+ are the same for a given line during the two different rotations. Those parameters have been collected in Table 6 for the three salts. The r parameter accounts in part for finite temperature effects ($r = 1$ at $T = 0$ K and $r = 0$ at $T = T_N$). Only its order of magnitude can be deduced from the fit. In the present case, $r \approx 1$ was found for all fits, in agreement with the value of T_N ($T_{\mathrm{Exp}}/T_{\mathrm{N}} \approx 0.5$). The Ω_- and Ω_+ values are close together within the series and comparable with values reported for other organic materials such as TMTTF or TMTSF salts or the organometallic $Cp^*Mo(dmit)_2^{\bullet}$ indicating a common origin of the anisotropy [22]. In these systems the magnetic anisotropy has two main origins [34], namely the spin-orbit coupling and the dipole-dipole interaction. We may think that both components are important because of the presence of large spin orbit coupling

Table 6. Magnetic experimental parameters obtained by AFMR at 4 K for $[Cp_2Modmit^{+\bullet}][X^-]$.

	T_N (K)	α (°)	B_- (Gauss)	B_+ (Gauss)
$[Cp_2Modmit^{+\bullet}][PF_6^-]$	11.5 ± 0.2	9 ± 1	6200 ± 100	7000 ± 100
$[Cp_2Modmit^{+\bullet}][AsF_6^-]$	9.5 ± 0.2	39 ± 1	6000 ± 100	7200 ± 100
$[Cp_2Modmit^{+\bullet}][SbF_6^-]$	7.5 ± 0.2	42 ± 1	5900 ± 100	6900 ± 100

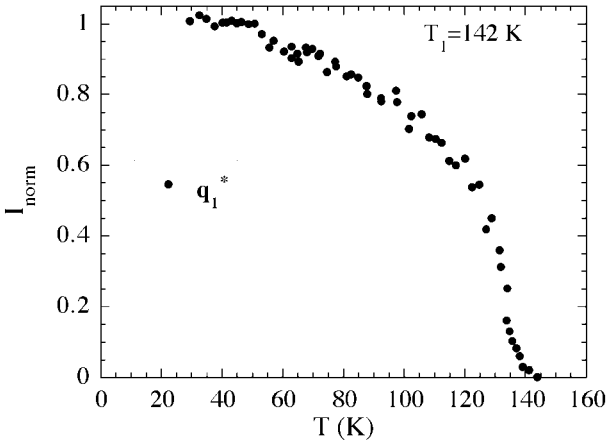

Fig. 11. Temperature dependence of the normalized (at saturation) intensity of one (0,1/2,1/2) superlattice reflexion in $[Cp_2Mo(dmit)^{+\bullet}][AsF_6^-]$.

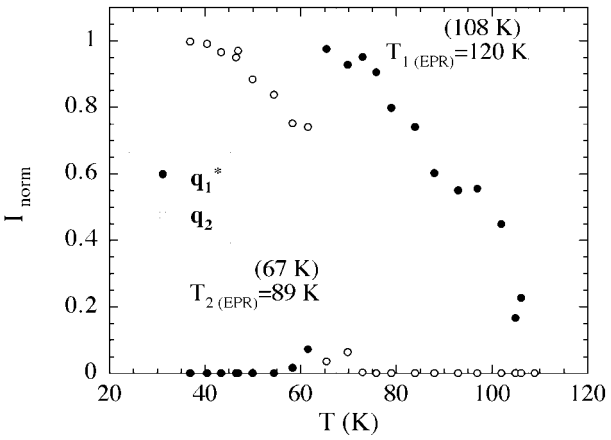

Fig. 12. Temperature dependence of the normalized (at saturation) intensity of two reflexions belonging to the $\mathbf{q}_1^* = (0, 1/2, 1/2)$ and $\mathbf{q}_2 = (0, 1/2, 0)$ superlattices for $[Cp_2Mo(dmit)^{+\bullet}][PF_6^-]$. The discrepancy with the transition temperatures determined by EPR is attributable to an experimental temperature measurement problem during the X-ray data collection.

(due to Mo atoms). However, a low temperature structure would be necessary for a more detailed quantitative discussion.

6 Discussion and conclusion

These combined structural and magnetic studies allowed us to identify two fully different behaviours for the PF_6^- and AsF_6^- salts. The anion disorder observed in the room temperature structure of each of the three salts is probably at the origin of the different phase transitions identified from the EPR linewidth temperature dependence and confirmed by low temperature X-ray studies. At this point, we may imagine that the superlattices with the $\mathbf{q}_1^*$

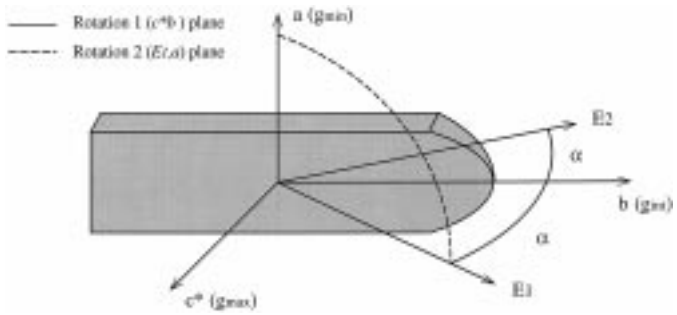

Fig. 13. The crystal shape and the position of the crystallographic and Easy axes (E_1, E_2).

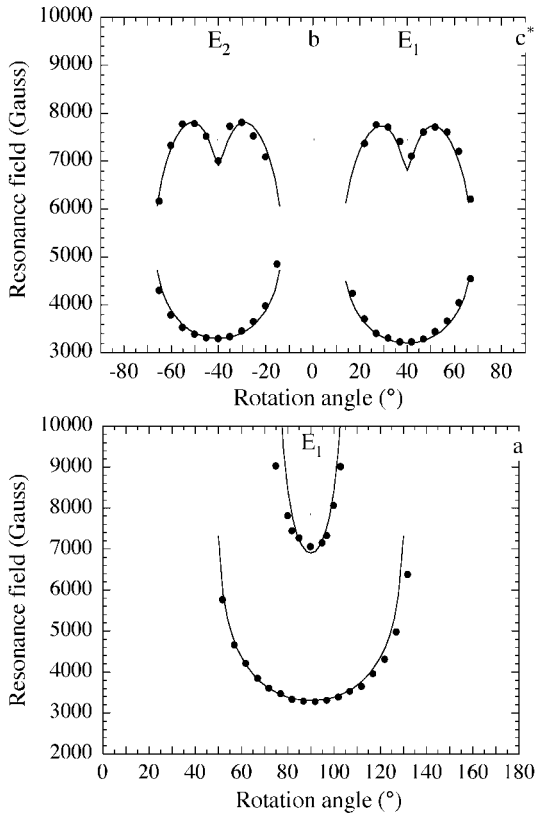

Fig. 14. AFMR rotation patterns in the (bc^*) and (aE_1) planes for $[Cp_2Mo(dmit)^{+\bullet}][AsF_6^-]$. The continuous lines gives the fit with the AFMR theory [29,30].

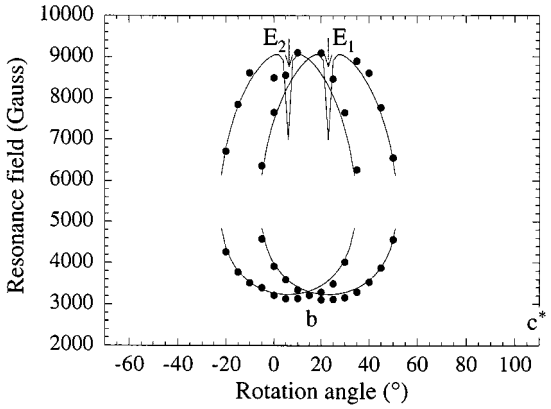

Fig. 15. AFMR rotation patterns in the (bc^*) plane for $[Cp_2Mo(dmit)^{+\bullet}][PF_6^-]$. The continuous lines gives the fit with the AFMR theory [29,30].

and $\mathbf{q}_2$ wave vectors follow from anion order-disorder transitions. This is further substantiated by the fact that the g factor is almost temperature independant, suggesting that the $Cp_2Mo(dmit)^{+\bullet}$ cation radicals do not move or distort significantly at the structural transitions. The different behaviour of the PF_6^- salt (compared to the AsF_6^- and SbF_6^- salts) is clearly related to different anion sizes. The evolution of the unit cell with the anion size has shown that the c parameter is the most affected one. It follows that the size of the anion site is almost constant in the a and b directions. Thus, the free volume of the cavity for the smaller anion (PF_6^-) is comparatively larger than for the bigger ones: the PF_6^- anion has more room to move around. This probably explains why the PF_6^- is able to stabilize into two different superlattices while the larger anions are more constrained in the structure and allow only one structural transition. Although these effects appear to be minor molecular modifications, they offer a novel original example of the relationship between the compacity of the crystal lattice and its capacity to distort. In these radical systems, this interplay also influences their electronic properties whose study can be effectively used as a probe of the structural modifications.

To gain a deeper understanding of those two different behaviours, solid solutions $[Cp_2Mo(dmit)^{+\bullet}][(AsF_6^-)_x (PF_6^-)_{1-x}]$ or $[Cp_2Mo(dmit)^{+\bullet}][(SbF_6^-)_x (PF_6^-)_{1-x}]$ incorparating the PF_6^- in one hand and the AsF_6^- or SbF_6^- anions on the other hand have been prepared and the corresponding phase diagrams are being actively investigated. We should then be able to answer how a system (the PF_6^- salt) with two successive phase transitions ($\mathbf{q}_1^*$ and $\mathbf{q}_2$) transforms – continuously or not – into a other system (the AsF_6^- or SbF_6^- salts) with only one transition ($\mathbf{q}_1^*$).

We thank F. Grelaud and D. Lepevelen (ICMCB, Pessac) for some low temperature X-ray diffraction experiments and J. Amiell (CRPP, Pessac) for his invaluable help with the EPR spectrometer. Discussions with J.P. Pouget (LPS, Orsay) and P. Batail (IMN, Nantes) are also gratefully acknowledged.

References

1. (a) K. Bechgaard, C.S. Jacobsen, K. Mortensen, H.J. Pedersen, N. Thorup, Solid State Commun. **33**, 1119 (1980); (b) K. Bechgaard, Mol. Cryst. Liq. Cryst. **79**, 1 (1982).
2. (a) D. Jérome, H.J. Shulz, Adv. Phys. **31**, 299 (1982); (b) C. Bourbonnais, D. Jérome, Science **281**, 1155 (1998).
3. M.J. Rosseinsky, J. Mater. Chem. **5**, 1497 (1995).
4. K. Tanigaki, K. Prassides, J. Mater. Chem. **5**, 1515 (1995).
5. J.M. Williams, J.R. Ferraro, R.J. Thorn, K.D. Carlson, U. Geiser, H.H. Wang, A.M. Kini, M.H. Whangbo, *Organic Superconductors* (Prentice-Hall, Englewood Cliffs, N.J., 1992).
6. A.M. Kini, U. Geiser, H.H. Wang, K.D. Carlson, J.M. Williams, W.K. Knok, K.G. Vandervoort, J.E. Thompson, D.L. Stupka, D Jung, M.H. Whangbo, Inorg. Chem. **29**, 2555 (1990).
7. (a) J.M. Williams, A.M. Kini, H.H. Wang, K.D. Carlson, U. Geiser, L.K. Montgomery, G.J. Pyrka, D.M. Watkins, J.M. Kommers, S.J. Boryschuk, A.V. Strieby Crouch, W.K. Knok, J.E. Schriber, D.L. Overmyer, D. Jung, M.H. Whangbo, Inorg. Chem. **29**, 3262 (1990); (b) U. Welp, S. Flesher, W.K. Kwok, G.W. Crabtree, K.D. Carlson, H.H. Wang, U. Geiser, J.M. Williams, V.M. Hitsman, Phys. Rev. Lett. **69**, 840, (1992); (c) K. Miyagawa, A. Kawamoto, Y. Nakazawa, K. Kanoda, Phys. Rev. Lett. **75**, 1174 (1995).
8. A. Kawamoto, K. Miyagawa, K. Kanoda, Phys. Rev. **55**, 14140 (1997).
9. M.H. Whangbo, J.M. Williams, A.J. Schultz, T.J. Emge, M.A. Beno, J. Am. Chem. Soc. **109**, 90 (1987).
10. M. Fourmigué, B. Domercq, I. Jourdain, P. Molinié, F. Guyon, J. Amaudrut, Chem. Eur. J. **4**, 1714 (1998).
11. M. Fourmigué, C. Lenoir, C. Coulon, F. Guyon, J. Amaudrut, Inorg. Chem. **34**, 4979 (1995).
12. The structures were solved by direct methods using the Xtal3.2 or SHELXTL chains of programs. H atoms were introduced at calculated positions, included in structure factor calculations but not refined. S.R. Hall, H.D. Flack, J.M. Stewart, Xtal3.2 Reference Manual (1992), Universities of Western Australia, Geneva and Maryland. G.M. Sheldrick, SHELXTL Ver 5.04 (1995), Siemens Analytical X-ray Instruments Inc., Madison, Wisconsin, USA.
13. Extended-Hückel type calculations were performed with double-ζ orbitals for C, Mo and S: (a) R.J. Hoffman, Chem. Phys. **39**, 1397 (1963); (b) M.H. Whangbo, J.M. Williams, P.C.W. Leung, M.A. Beno, T.J. Emge, H.H. Wang, K.D. Carlson, G.W. Crabtree, J. Am. Chem. Soc. **105**, 5815 (1985); (c) E. Clementi, C. Roetti, At. Nucl. Data Tables **14**, 177 (1974).
14. The Curie constant normalized to $C_0 = 0.375$ (the expected value for one mole of spin 1/2) amounts to 0.7, 0.9 and 1.0 in the PF_6^-, AsF_6^- and SbF_6^- salts respectively. The low value found in the PF_6^- salt is probably attributable to the lower quality of the crystals of this compound.
15. J.B. Torrance, *Chemistry and Physics of One-Dimensional Metals*, edited by H.J. Keller (NATO ASI Series, B25, Plenum Press, New-York, 1977), p. 137.
16. J. Hubbard, Phys. Rev. B **17**, 494 (1978).
17. C. Uyeda, M. Date, J. Phys. Soc. Jpn **55**, 2830 (1986).
18. L. Landau, E. Lifchitz, *Elasticity Theory* (Mir, Moscou, 1967).

19. PF_6^- salt : $g_a = 1.9999$, $g_b = 2.0276$ and $g_c = 2.0133$
AsF_6^- salt : $g_a = 2.0000$, $g_b = 2.0271$ and $g_c = 2.0135$
SbF_6^- salt : $g_a = 2.0000$, $g_b = 2.0278$ and $g_c = 2.0137$.
20. P. Baillargeon, C. Bourbonnais, S. Tomic, P. Vaca, C. Coulon, Synth. Met. **27**, B83 (1988).
21. C. Coulon, A. Maaroufi, J. Amiell, E. Dupart, S. Flandrois, P. Delhaès, R. Moret, J.P. Pouget, J.P. Morand, Phys. Rev. B **26**, 6322 (1982).
22. C. Coulon, unpublished result.
23. A.K. Pal, Indian J. Pure Appl. Phys. **34**, 681 (1996).
24. C. Coulon, P. Delhaès, S. Flandrois, R. Langnier, E. Bonjour, J.M. Fabre, J. Phys. France **43**, 1059 (1982).
25. R. Laversanne, J. Amiell, P. Delhaès, D. Chasseau, C. Hauw, Solid State Commun. **52**, 177 (1984).
26. C. Coulon, C. Livage, L. Gonzalez, K. Boubekeur, P. Batail, J. Phys. I France **3**, 1153 (1993).
27. P. Batail, C. Livage, S.S.P. Parkin, C. Coulon, J.D. Martin, E. Canadell, Angew. Chem., Int. Ed. Engl. **30**, 1498 (1991).
28. C. Coulon, R. Laversanne, J. Amiell, J. Physica **143B**, 425 (1986).
29. M. Fourmigué, C. Coulon, Adv. Mater. **6**, 948 (1994).
30. R. Laversanne, C. Coulon, J. Amiell, J.P. Morand, Europhys. Lett. **2**, 401 (1986).
31. C. Coulon, J.C. Scott, R. Laversanne, Phys. Rev. B **33**, 6235 (1986).
32. T. Nagamiya, K. Yosida, R. Kubo, Adv. Phys. **4**, 1 (1955).
33. T. Nagamiya, Prog. Theor. Phys. **11**, 309 (1954).
34. M. Roger, J.M. Delrieu, E. Wope Mbougue, Phys. Rev. B **34**, 4952 (1986).